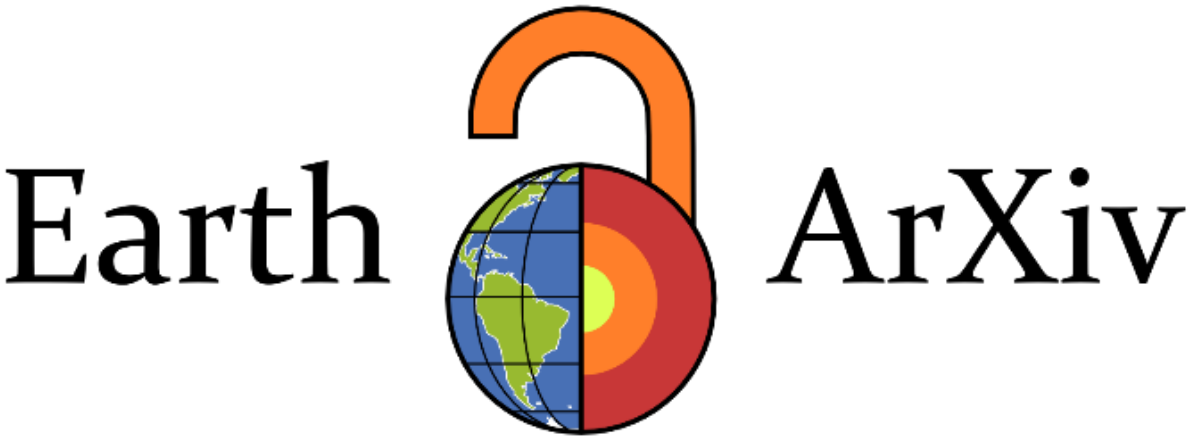

Reconciling remote sensing and reanalysis land surface temperatures: How surface conditions shape bias between GOES-16 and MERRA-2 across the contiguous US

Dhruva Kathuria,[a,b] Alexandra G. Konings,[c] Jana Kolassa,[b,d,e] Yanlan Liu,[f,g] Meng Zhao,[h] Alexey N Shiklomanov[b]

[a] *GESTAR II, Morgan State University, Baltimore, MD*

[b] *Global Modeling and Assimilation Office, NASA Goddard Space Flight Center, Greenbelt, MD*

[c] *Department of Earth System Science, Stanford University, Stanford, CA*

[d] *Science Systems and Applications, Inc., Lanham, MD*

[e] *European Centre for Medium-Range Weather Forecasts, Bonn, Germany*

[f] *School of Environment and Natural Resources, The Ohio State University, Columbus, OH*

[g] *School of Earth Sciences, The Ohio State University, Columbus, OH*

[h] *Department of Earth and Spatial Sciences, University of Idaho, Moscow, ID*

Corresponding author: Dhruva Kathuria, dhruva.kathuria@nasa.gov

ABSTRACT

Land surface temperature is a key variable governing land–atmosphere energy and water exchanges. Despite its importance, satellite observations and reanalysis products often differ in how they define the effective depth of land surface temperature and in the assumptions underlying their estimates, making comparisons and interpretation challenging. In this study, we present a detailed comparison of land surface temperature from GOES-16 (satellite) and MERRA-2 (reanalysis) across the contiguous United States for 2022 and 2023. The results reveal systematic diurnal and seasonal biases: GOES-16 tends to be warmer than MERRA-2 in the afternoon and at night, but cooler in the morning. The magnitude of these biases varies by season. At night, GOES-16 is warmest relative to MERRA-2 for forests; in the morning, it is coolest for croplands and grasslands; and in the afternoon, it is warmest for barren and shrublands. Within individual land cover types, variability in surface conditions—such as soil moisture and elevation—modulates the bias at night and in the morning, with GOES-16 LST being warmer at night and cooler in the morning for wetter soils and at higher elevations. Our analysis also indicates that Leaf Area Index plays a role in bias patterns during spring and autumn, likely due to the association of temperature with leaf emergence and senescence. These findings provide new insights into the mechanisms underlying land surface temperature bias patterns and highlight the importance of accounting for surface condition variability in bias correction and data assimilation workflows.

1. Introduction

Land surface temperature (LST) represents the temperature of the top layer of the earth's surface encompassing soil, vegetation or other surface features. As a key variable in land-atmosphere interactions, LST regulates the exchange of energy and water between the surface and the atmosphere (Li et al., 2023; Norman & Becker, 1995). Its significance extends across various disciplines, playing a crucial role in phenology and the carbon cycle (Zhang et al., 2007), soil moisture estimation (Gallego-Elvira et al., 2019; Zhao et al., 2021), evapotranspiration modeling (Kalma et al., 2008), drought monitoring (Karnieli et al., 2010), geology (Watson, 1975), and urban heat island assessment (Peng et al., 2018). Despite its importance, global scale LST

measurements and model products differ in the depths over which LST is averaged and in their underlying assumptions, leading to uncertainties in their comparability and interpretation.

Remote sensing satellites provide an efficient and scalable method to retrieve LST on a global scale. Among them, thermal infrared satellites have demonstrated strong performance in terms of both accuracy and spatiotemporal resolution (Jia et al., 2024). Thermal infrared-derived LST is commonly referred to as skin LST due to its shallow penetration depth (for both soil and vegetation canopy), which typically ranges from 1 to 100 μm. LST retrievals in the thermal infrared region are often performed using semi-empirical algorithms that determine LST as a function of top-of-atmosphere brightness temperatures while incorporating surface emissivity and atmospheric conditions as key constraints (Li et al., 2023). Geostationary satellites, due to their high frequency sampling from 15 minutes to 1 hour, can characterize the LST diurnal temperature curve of a pixel, though at a coarser resolution than orbiting satellites (Freitas et al., 2013). However, thermal infrared-derived LST are affected by cloud contamination (e.g. Figure 1a), which substantially restricts data availability. Alternatively, reanalysis products—which update land surface models states with multi-source observations through data assimilation (Baatz et al., 2021)— provide LST estimates with spatiotemporal continuity in all-weather conditions (Jia et al., 2024). However, this advantage comes at the cost of coarser spatial resolution compared to satellite-based products (e.g. Figure 1a). To maximize the benefits of both satellite-derived and reanalysis-derived LST while mitigating their respective limitations, there has been significant interest in integrating remote sensing observations with reanalysis products through downscaling (Jia et al., 2022) or data fusion/assimilation techniques (Bateni et al., 2013; Caparrini et al., 2003; Dong et al., 2022; Ghent et al., 2010; Lu et al., 2017; Meng et al., 2009; Olivera-Guerra et al., 2025). Such approaches aim to generate all-weather LST datasets and enhance the simulation of water and energy fluxes.

Combining these data sources, however, is challenging due to differing modeling assumptions and the strong influence of land surface conditions on both thermal infrared satellite retrievals and reanalysis LST estimates. For example, reanalysis-derived skin LST can be biased by differences in the depth over which LST is averaged, leading to potential discrepancies when compared with in situ measurements or satellite-based LST (Wang et al., 2022). Ancillary data

on land cover, elevation, soil texture, Leaf Area Index (LAI), and other surface properties are important inputs to both reanalysis products and satellite retrieval algorithms, but differences in these input datasets can lead to differences in LST estimates. Land surface heterogeneity also influences thermal infrared retrievals: satellite-derived LST can be affected by variations in land cover, vegetation (Guillevic et al., 2013; Inamdar et al., 2008; Lagouarde et al., 2000), soil moisture (Friedl & Davis, 1994; Sun & Pinker, 2004), elevation (Beale et al., 2020; Ma et al., 2021), and soil texture (Müller et al., 2016; Wang et al., 2015). Additionally, thermal infrared LST retrievals depend on surface emissivity—used either as an input or estimated alongside LST—which itself varies with seasonality, land cover type, soil moisture, soil texture, vegetation density, and vegetation structure (Jin & Liang, 2006; Mira et al., 2010).

Thus, satellite-derived and reanalysis-based LST can differ substantially in their representation of skin LST across times of day, seasons, and varying surface conditions. However, the effects of these conceptual and structural differences remain poorly understood. Examining the spatiotemporal differences between skin LST from thermal infrared satellites and reanalysis products, as well as assessing the influence of land surface conditions on these differences, is a critical step toward improving bias correction, data fusion, and ultimately the assimilation of thermal infrared LST into land surface models. Here, we compare thermal satellite estimates of skin LST from the Geostationary Operational Environmental Satellite-16 (GOES-16; Yu et al. (2012); Yu & Yu (2020)) to reanalysis estimates of skin LST from the Modern-Era Retrospective Analysis for Research and Applications, version 2 (MERRA-2; Gelaro et al. (2017)). While we expect GOES-16 and MERRA-2 to exhibit broadly consistent spatial and temporal patterns, we anticipate notable differences in magnitude. Specifically, due to its greater representative depth, we hypothesize that MERRA-2 has a more muted and lagged diurnal cycle than GOES-16 does. We expect these biases to be more pronounced in vegetated areas, as GOES-16 observes only the top few millimeters of vegetation, whereas MERRA-2 integrates the entire canopy and the top few cm of soil. Additionally, we expect substantial variations between these datasets in mountainous regions due to the impact of topography on thermal infrared retrievals. While previous studies (e.g. (Ma et al. (2021)) have assessed the accuracy of individual remote sensing and reanalysis LST products using in situ data, we are not aware of any that have directly compared these datasets to better understand their differences and the role of land surface

conditions in shaping them. Furthermore, seasonal effects of surface controls on LST accuracy have not been fully considered. This study aims to address two key questions:

(a) Are there systematic differences between GOES-16 and MERRA-2 LST and, if so, how do they vary across space and time?

(b) Which land surface characteristics are most likely to drive substantial LST differences between GOES-16 and MERRA-2?

2. Study Area

The study area encompasses the contiguous United States, which was selected because GOES-16 LST has been extensively validated across diverse land covers in this region using in situ measurement from the National Oceanic and Atmospheric Administration's (NOAA) Surface Radiation Budget network (Augustine & Dutton, 2013; Yu et al., 2012), providing greater confidence in the product's accuracy. Additionally, GOES-16 LST is available at a high resolution of 2 km for the contiguous United States (compared to 10 km for the full disk coverage) (Yu et al., 2012; Yu & Yu, 2020). The study focuses on four months—January, April, July, and October—for the years 2022 and 2023. These months are assumed to be representative of the winter, spring, summer, and fall seasons, respectively. Conducting the analysis for all months or more than two years was not feasible due to computational constraints. The analysis is restricted to the years 2022 and 2023 because product quality information, critical for filtering out low-quality GOES-16 retrievals, was not available for earlier years at the time of this study.

3. Data

a. MERRA-2 LST

MERRA-2 is the National Aeronautics and Space Administration's (NASA) state-of-the-art reanalysis product, developed by the Global Modeling and Assimilation Office (Gelaro et al., 2017). MERRA-2 provides simulations of skin LST along with various land surface estimates—including soil moisture, streamflow, terrestrial water storage, and snow (Reichle et al., 2017).

While numerous studies have examined the use of MERRA-2 near-surface air temperature (Gupta et al., 2020; Huang et al., 2023) in various applications, the skin LST product remains largely underused by the broader scientific community. The Catchment Land Surface Model (Koster et al., 2000) governs land surface processes within the MERRA-2 reanalysis framework. This model divides the continental surface into hydrological catchments, varying in size from a few kilometers to approximately 250 km, with the boundaries defined by topography. Each MERRA-2 grid cell (~ $0.625^{o} \times 0.5^{o}$ spatial resolution) contains one or more of these irregularly shaped catchments, and some catchments span multiple MERRA-2 pixels. Each catchment is divided into areas that are either saturated, unsaturated, or wilting, and the fractional areas in each of these states are dynamically adjusted based on the catchment's total water content. The surface energy balance — including LST — is calculated separately for each of these areas, and the skin LST of each MERRA-2 pixel is calculated as an area-weighted average of these LSTs within that pixel. The LST is representative of a composite surface layer with a finite and constant soil layer heat capacity (70,000 J kg^{-1} K^{-1}), encompassing both the vegetation canopy and approximately the top 5 cm of the soil (except for tropical forests; Koster et al. (2020)).

b. GOES-16 LST

Thermal infrared skin LST derived from the Advanced Baseline Imager onboard GOES-16 (Yu et al. (2012); Yu & Yu (2020); ABI L2+ LST) is available at a 2 km hourly resolution for the contiguous United States and has reached provisional maturity, demonstrating stable accuracy based on ground validation studies (Yu et al., 2012; Yu & Yu, 2020). The Advanced Baseline Imager in GOES-16 has 16 spectral bands, out of which infrared bands 14 (centered at 11.2 μm) and 15 (centered at 12.3 μm) are used for LST retrieval using the split-window technique (Yu et al., 2008). Assuming we have a good estimate of surface emissivity, the split window technique is a semi-empirical approach that uses the difference between top-of-atmosphere brightness temperature measurements of these two bands to provide an atmospheric correction. The split-window technique used in GOES-16 is computationally efficient and has been shown to reduce sensitivity to uncertainties in emissivity, water vapor and satellite zenith angle, which are the biggest sources of errors in thermal infrared LST retrievals (Yu et al., 2012). To account for differences in LST retrievals caused due to atmospheric water content as well as differences in

discontinuity between LST and air temperatures during daytime and nighttime, the regression coefficients for the split-window equation have been specified uniquely for four different scenarios: day with dry atmosphere, day with moist atmosphere, night with dry atmosphere, night with moist atmosphere (Yu et al., 2012; Yu & Yu, 2020).

c. Land surface data

We use 17 land cover classes defined by the International Geosphere-Biosphere Programme (IGBP) based on the Moderate Resolution Imaging Spectroradiometer (MODIS) Land Cover Type product (Friedl & Sulla-Menashe (2022); MCD12Q1, Version 6.1), available at a 500 m spatial resolution. Elevation data are obtained from the Shuttle Radar Topography Mission (Farr & Kobrick (2000); SRTM GL1) at 30 m resolution. Percent clay content is derived from the gridded Soil Survey Geographic database (Staff, 2020), also at 30 m spatial resolution. Additionally, we use MERRA-2 hourly surface soil moisture (5 cm depth) and climatological prescribed LAI fields derived from the Advanced Very High Resolution Radiometer (and provided within the MERRA-2 reanalysis), both at a spatial resolution of 0.625° × 0.5°.

4. Methods

We computed the hourly differences between the two datasets at the spatial resolution of MERRA-2 across the diurnal cycle and averaged them temporally over January, April, July, and October. To assess how surface conditions influence these differences, we analyzed them with respect to five land surface drivers: land cover, LAI, soil moisture, elevation, and clay content (a proxy for soil texture). To interpret these relationships, we first identified the primary driver of bias variability — the variable that explains the largest proportion of spatial variation in bias. We then examined how the remaining variables contribute to explaining the residual variability.

a. Preprocessing

1. LST DATA

We reproject the GOES-16 LST data from the geostationary satellite view projection to the WGS84 geographic projection (EPSG: 4326) to align it with MERRA-2. We use bilinear interpolation to reproject the LST values and apply nearest-neighbor interpolation to reproject the product quality information flags.

The product quality information includes flags for LST quality, which indicate categories such as no retrieval, low quality, medium quality, and high quality. It also includes flags for land surface type (land, snow/ice, inland water, and coastal) and cloud conditions (clear, probably clear, probably cloudy, and cloudy). We treat inland water pixels as land and generate retrievals over snow/ice. However, most coastal regions (99%) contain no retrievals. To prevent potential errors from including coastal water pixels, we exclude all GOES-16 pixels flagged as coastal from the analysis. The product does not provide retrievals under cloudy conditions. Pixels flagged as low-quality LST are those that meet any of the following conditions: (1) probably cloudy skies, (2) presence of thin cirrus clouds, (3) atmospheric optical depth greater than 1.0, or (4) active fire within the pixel. We exclude all GOES-16 pixels flagged as low-quality LST from the analysis.

We linearly aggregate the GOES-16 pixels to MERRA-2 resolution by assuming that a GOES-16 pixel is entirely contained within a MERRA-2 pixel if its center coordinate lies within the extent of the MERRA-2 pixel. Since the split-window algorithm used by GOES-16 determines LST as a linear function of the brightness temperatures (Yu, Tarpley, Xu, et al., 2012; Yu & Yu, 2020), we do not expect that directly aggregating LST values linearly to match the MERRA-2 resolution will introduce significant errors. Direct linear aggregation of satellite-derived LST to the spatial resolution of land surface models has also been commonly employed in previous studies (Ghent et al., 2010; R. H. Reichle et al., 2010). To ensure a fair comparison between the two LST products, we include only those MERRA-2 pixels that contain at least 85% valid GOES-16 LST pixels flagged as medium or high quality and non-coastal. This criterion limits

the combined contribution of cloudy and probably cloudy pixels to a maximum of 15% of the total MERRA-2 pixel area. Both MERRA-2 and GOES-16 data are provided in Coordinated Universal Time (UTC). We perform the diurnal analysis in local time by converting the UTC timestamps to local time, using the center coordinate of each MERRA-2 pixel.

2. LAND SURFACE CONTROLS

We consolidate several land cover classifications into broader composite categories to ensure adequate pixel representation within each group. Specifically, we group cropland and cropland/natural vegetation into a single "cropland" category; closed and open shrublands into "shrubland"; all forest types—evergreen needleleaf, evergreen broadleaf, deciduous needleleaf, deciduous broadleaf, and mixed forest—into "forest"; and woody savannas and savannas into "savanna." We conduct the land cover-based analysis using the dominant classification within each MERRA-2 pixel, defined as the land cover type occupying at least 50% of the pixel area. We assign a 500 m land cover pixel to a MERRA-2 pixel if its center coordinate falls within the MERRA-2 pixel boundary. We exclude MERRA-2 pixels dominated by water, snow and ice, or urban areas, as our analysis focuses on land surface covariates. When analyzing the influence of dominant land cover on LST bias (Section 5.2), we also exclude pixels classified as permanent wetlands due to their limited representation (only three pixels within contiguous United States). Additionally, we exclude mixed land cover pixels—those where no single land cover type exceeds 50%—from Section 5.2, as their high variability prevents the generalization of bias patterns across surface conditions. However, we retain these pixels in the broader analysis in Section 5.1.

For the land cover analysis, we focus on six dominant land cover types: barren land, cropland, forest, grassland, savanna, and shrubland (Figure 3a). In interpreting the results, we combine barren land (38 pixels across contiguous United States) and shrubland (172 pixels) due to predominantly low LAI values for pixels with shrublands as dominant landcover—more than 90% of the shrubland pixels across the two years have an LAI less than 1 representing sparse vegetation cover. For the remaining surface controls—elevation, LAI, soil moisture, and clay

content—we compute mean values by applying a linear spatial average at the MERRA-2 spatial resolution.

b. Statistical metrics

Bias is an effective measure for assessing the systematic spatial differences between two datasets (e.g., (Ma et al., 2021). It may arise from factors such as differences in vertical depths and modeling assumptions. We define the bias between GOES-16 and MERRA-2 as:

$$\text{Bias} = \text{E}(\text{LST}_\text{G} - \text{LST}_\text{M})$$

where E denotes the expectation, LST_G represents the upscaled GOES-16 LST for a MERRA-2 pixel, and LST_M is the corresponding MERRA-2 LST. We calculate the expectation separately for each month and hour by first computing the LST differences between GOES-16 and MERRA-2 for each hour across all available days (subject to quality control constraints in Section 4.1.1) within a month, and then averaging these differences. We compute a pixel's bias only if it contains data for at least five days in a given hour and month. Although this threshold may appear low, Figure S1 (Supporting Information) shows no significant differences in bias based on the number of available days per month, and most pixels in the analysis contain a higher number of days for each time period. In the land cover analysis (Section 5.2), we calculate the bias for each dominant land cover type and then spatially average it within that class. In Section 5.3, we do not spatially average the bias; instead, we examine how its spatial variability relates to different land surface controls.

To streamline the discussion of results, we temporally average the bias over three key time periods: night (12 AM–3 AM), morning (8 AM–11 AM), and afternoon (2 PM–5 PM). These time periods were selected because they represent critical phases of the LST diurnal cycle. Additionally, for the selected morning and afternoon periods, the negative and positive bias peaks consistently fell within these intervals across all seasons. For an hour and month, to identify the percent of spatial variability in bias explained by a surface control, we use the one-way Analysis of Variance (ANOVA) for landcover, and the coefficient of determination for the rest of the surface controls.

We quantify the linear association between a surface control and spatial bias (Section 5.3) using the Pearson correlation coefficient (R). We calculate R for each time period (night, morning and afternoon), month, and land cover type by pooling all spatial pixels with bias values—computed only when the criteria outlined above are satisfied—across the two study years. For each pixel, we linearly average the corresponding surface control over the selected time interval and month for each year separately, and then correlate the time period specific monthly means with the bias. While there is no universal guideline for interpreting the strength of correlation, we classify it as moderate if R is between 0.4 and 0.6, and strong if R exceeds 0.6.

5. Results

a. Diurnal and seasonal variation in bias

GOES-16 is warmer (positive bias) or cooler (negative bias) than MERRA-2 depending on the time of day (Figure 1b). Across seasons and years for the entire contiguous United States, GOES-16, on average, is 1K warmer than MERRA-2 at night, 1K colder in the morning, and 3K warmer in the afternoon. For a particular time period, the magnitude of this spatially-averaged bias varies across seasons, with year-to-year variability between 2022 and 2023 relatively minimal (Figure 1b). The average morning negative bias is the highest for July (-2.3K) and lowest for October (-0.52K) while the average afternoon positive bias is highest for April (5.2K) and lowest for January (1.8K). The average night bias remains similar across seasons.

Spatial variation in the bias also varies with the time of day and season (Figure 2 and Figure S2; Supporting Information). At night, across all seasons, the majority of pixels exhibit a bias within the ±2K range, with most pixels showing GOES-16 LST warmer than MERRA-2. A significant proportion of pixels display a bias of more than +2K, with January (33%) and April (31%) showing the highest percentages of such pixels. The highest spatial variation in bias (standard deviation = 2.7K) occurs in January while the least variation occurs in July (standard deviation = 1.6K). Regionally, the west and east coasts tend to exhibit positive biases, while central areas more often display negative biases. The western U.S. mountain regions—including the Rocky

Mountains, Colorado Plateau, and Sierra Nevada—show particularly elevated positive biases in January.

In the morning, most pixels exhibit GOES-16 LST cooler than MERRA-2, with the majority falling within a bias range of ±2K for January (59%), April (77%), and October (84%). July shows the highest percentage of pixels (64%) where GOES-16 LST is cooler than MERRA-2 by at least 2K. The overall spatial variation in morning bias exhibits a pattern similar to that observed at night, with January exhibiting the highest variation (standard deviation = 2.8K) and July the least (standard deviation = 1.5K). The spatial patterns in the morning vary with season. Spatial patterns of bias shift seasonally: the mountainous western regions maintain positive biases in January, while July shows more spatially uniform patterns. In October, the west coast tends to exhibit modest positive biases.

In the afternoon, GOES-16 is warmer than MERRA-2 for most pixels across all seasons (Figure S2; Supporting Information). A substantial proportion of pixels exceed a +2K bias, with April showing the highest percentage (91%), followed by October (64%). July has the highest variability in bias (standard deviation = 3.7K) with October having the least variability (standard deviation = 1.7K). Spatially for January, GOES-16 has widespread warmer biases across the western, southern, and eastern U.S., while the central-northern region tends to have cooler biases. In July, a pronounced east–west gradient emerges: western regions generally exhibit warmer GOES-16 biases, whereas eastern regions show cooler biases.

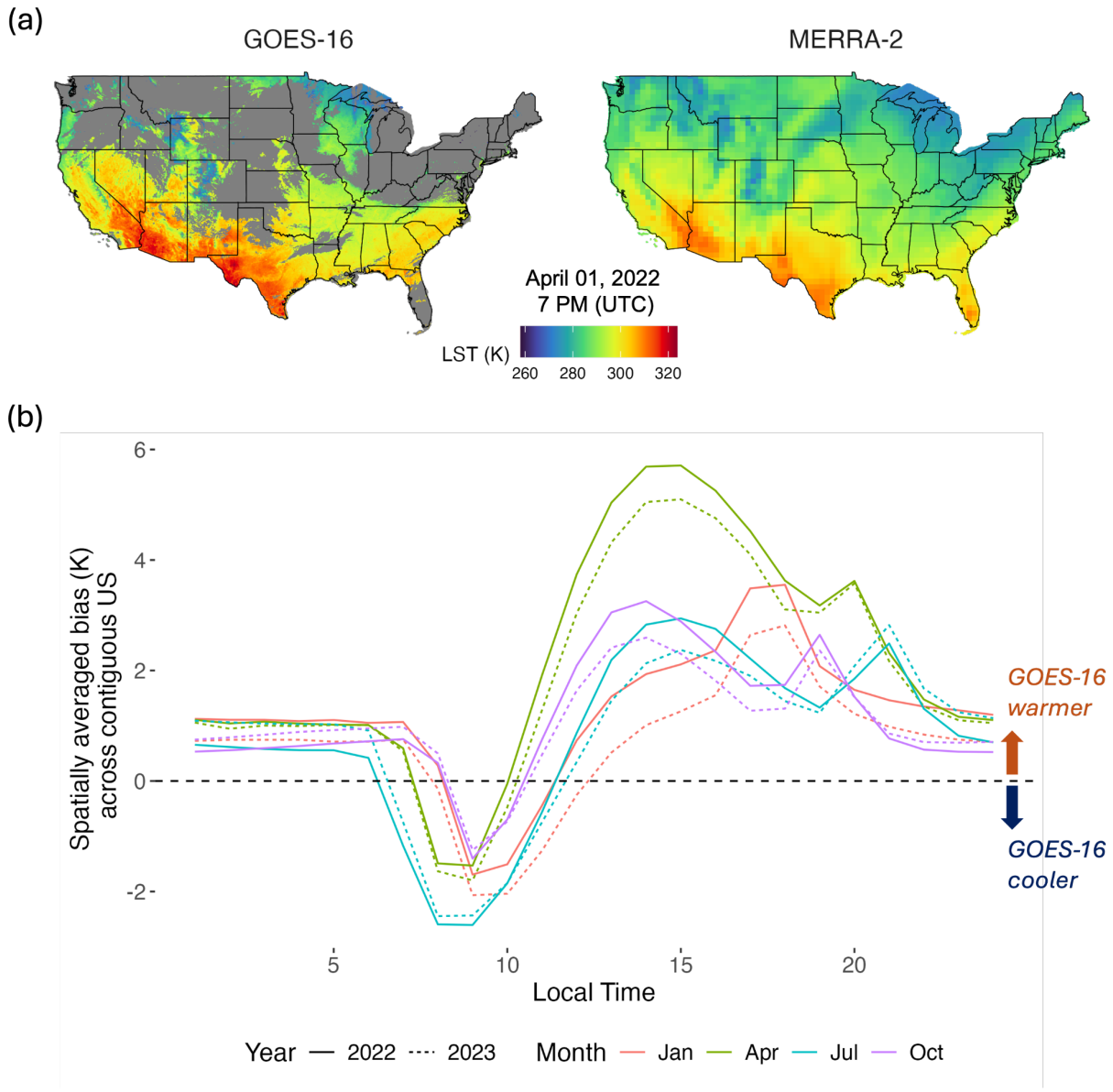

Figure 1. (a) Comparison of 2 km land surface temperature (LST) derived from GOES-16 with the reanalysis product MERRA-2 at approximately 0.625° ×0.5° resolution. GOES-16 LST is influenced by cloud cover, resulting in partial observation of contiguous United States at any given hour, whereas MERRA-2 LST, being a reanalysis product, provides complete coverage for each grid cell at every hour. (b) Spatially averaged over the entire contiguous United States for four selected months, the bias varies throughout the day, showing a positive bias (GOES-16 warmer than MERRA-2) during the night, a negative bias (GOES-16 cooler than MERRA-2) in the morning, and a pronounced positive bias during the afternoon.

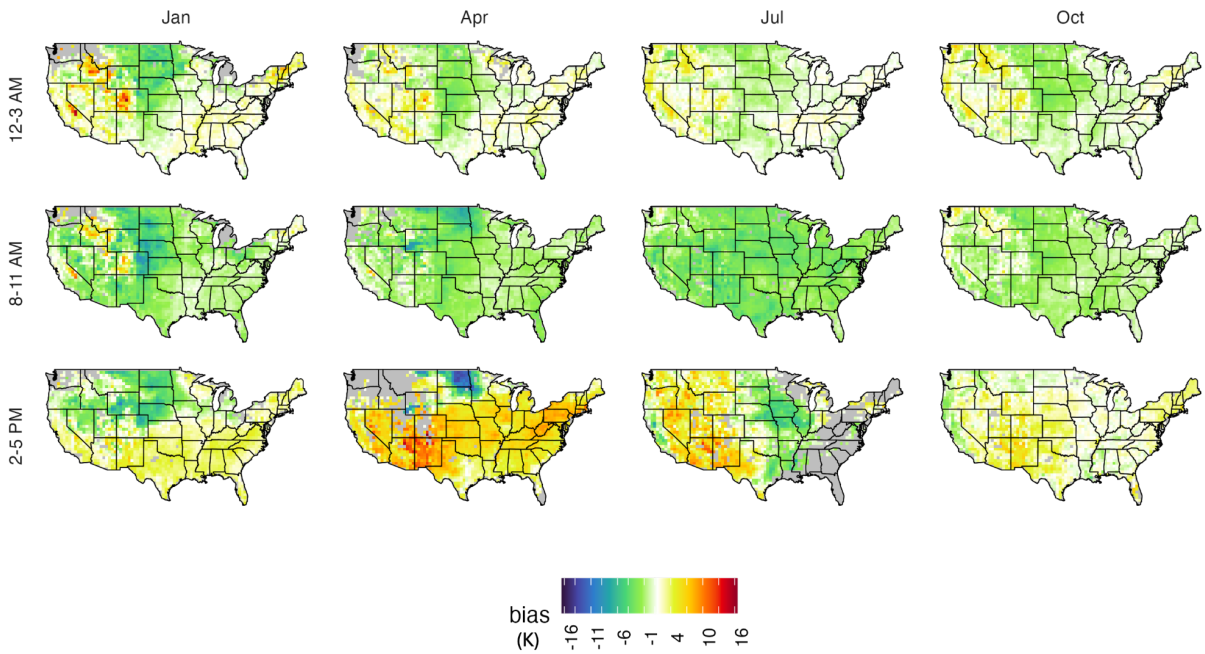

Figure 2. Spatial bias plots averaged across the two years for three time periods. Across contiguous United States, the spatial patterns of the bias between GOES-16 and MERRA-2 LST differ significantly across the night (12 AM–3 AM), morning (8 AM–11 AM), and afternoon (2 PM–5 PM) periods, as well as across the four months analyzed. For each time-period and month combination, there are regions where the bias deviates substantially from the spatially-averaged mean bias shown in Figure 1(b).

b. Bias across land covers

We identify the primary surface driver for each hour and month, and find that land cover is the dominant driver of bias variation across contiguous United States 78% of the time, explaining an average of 22% of the spatial variation in bias.

During the night, forests, savannas, barren areas, and shrublands predominantly exhibit GOES-16 LST warmer than MERRA-2, with a substantial subset exceeding an average bias of +2K (Figure 3, Figure S2; Supporting Information). Forests show the highest positive biases, with seasonal spatial averages ranging from 1.9K to 2.7K and the highest proportion of pixels (34%–67% across the four months) exceeding a +2K average bias. In contrast, croplands consist of a notable proportion of pixels where GOES-16 LST is cooler than MERRA-2 by at least −2K,

particularly in January (24%), April (18%), and October (21%). The seasonal variability in bias within specific land cover types is relatively low.

For morning, across land cover types, most pixels exhibit cooler GOES-16 LST compared to MERRA-2, except for forests, where more pixels show warmer GOES-16 LST in January (55%) and October (56%). Croplands and grasslands display the highest spatially-averaged negative biases, ranging from −0.8K to −2.6K across seasons. For all land covers except forests, bias variability across land covers in July is minimal, with average values ranging from −2.2K to −2.6K.

During the afternoon, barren and shrubland regions show the highest spatially-averaged biases, ranging from 3.8K to 7.9K, with the largest values in April (7.9K), followed by July (6.9K). Croplands record the lowest spatially-averaged biases, near-neutral in January (0.5K) and moderate in April (3.3K). Savannas and forests exhibit lower biases in July (0.6K and 1.3K, respectively) and October (2K and 1.5K, respectively). Notably, croplands in July exhibit an average negative bias of −1.4K. Aside from the effect of a pixel's dominant land cover type on the LST bias, we also examined the effect of land cover heterogeneity, defined as the number of different land cover types within a MERRA-2 pixel. However, we found that it had no significant impact on the bias.

c. Drivers of spatial bias variation within land covers

While land cover type is the primary factor contributing to spatial variation in LST bias, significant spatial variability also occurs within individual land cover types (Figure 4). These variations are largely driven by differing land surface conditions, including soil moisture, elevation, LAI, and clay content, within the same land cover (Figure 5). The influence of these conditions varies depending on the season and time of day, highlighting the dynamic relationship between surface characteristics and bias patterns within a land cover.

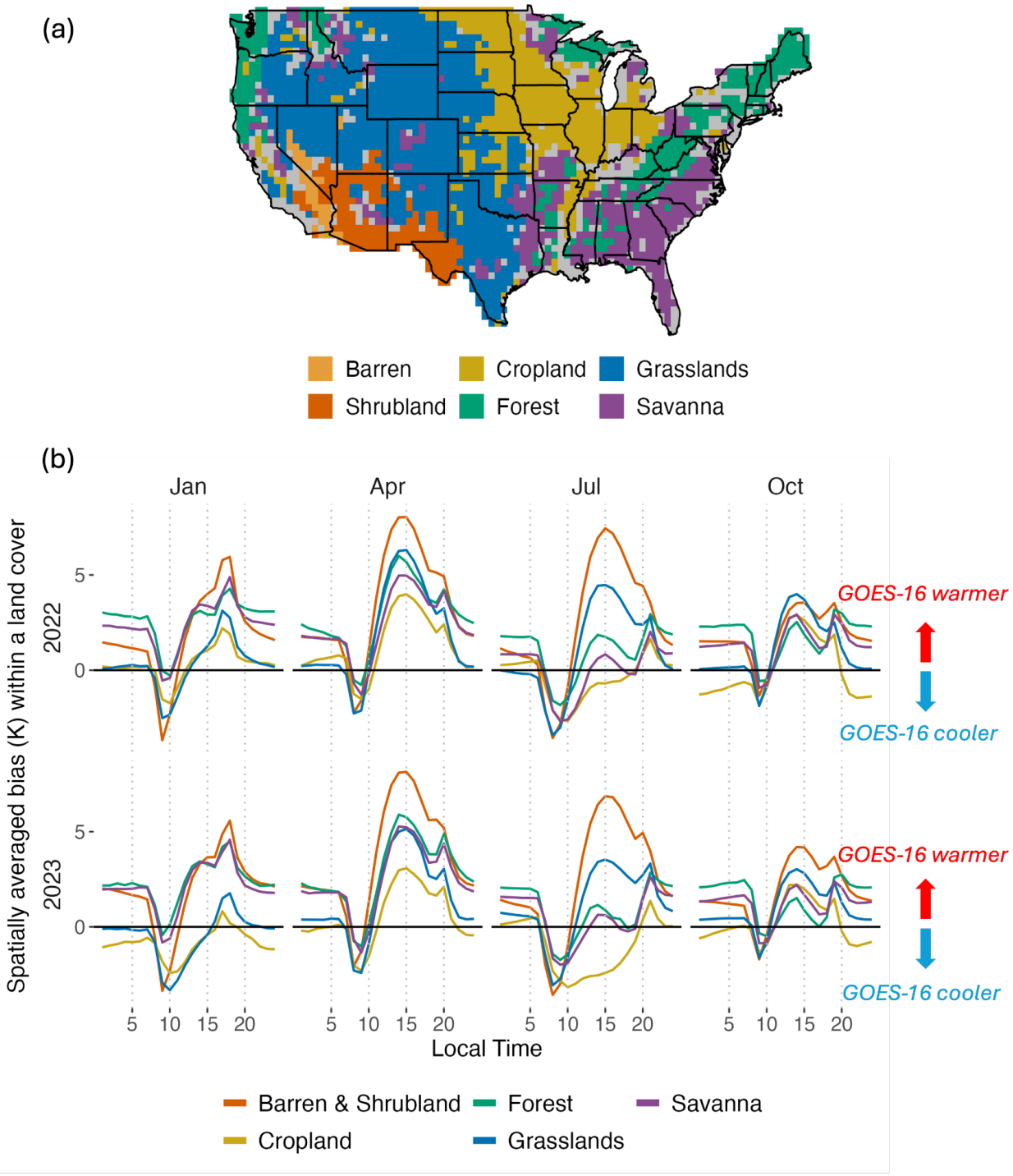

380
381
382 *Figure 3. (a) The six dominant land cover types at MERRA-2 resolution, defined as having at least 50%*
383 *of a specific MODIS 500 m land cover classification within a MERRA-2 pixel, analyzed in this study*
384 *across the contiguous United States. Gray regions indicate pixels where no dominant land cover exists or*
385 *where the dominant land cover is water, snow and ice, or urban areas. (b) For each season, the spatially-*

averaged diurnal bias varies significantly by land cover. At night, GOES-16 is warmest relative to MERRA-2 for forests; in the morning, it is coolest for croplands and grasslands; and in the afternoon, it is warmest for barren and shrublands. Generally, the magnitude of afternoon bias between the two datasets is higher than night. For each month, the diurnal bias depicted here is spatially averaged over the respective dominant land cover pixels across the entire contiguous United States.

During nighttime, spatial variability in bias within land cover types is significantly influenced by elevation and soil moisture. GOES-16 is consistently warmer than MERRA-2 in croplands year-round, with the magnitude of this bias strongly increasing with soil moisture; in grasslands and in barren and shrubland regions, the bias moderately increases with soil moisture during the winter and spring months (January and April). Elevation also plays a key role: bias increases strongly with elevation in forests (April, July, and October), moderately in grasslands (all months), and moderately to strongly in savannas (all months). In contrast, croplands exhibit a moderate to strong decrease in bias with increasing elevation throughout the year. This inverse relationship may be due to the negative correlation between elevation and soil moisture in croplands (January: -0.72, April: -0.71, July: -0.47, October: -0.37). LAI influence is primarily observed during the fall (October), when biases increase strongly with LAI levels in croplands, and moderately in forests and grasslands.

During the morning, spatial variation in LST bias is most strongly correlated with soil moisture, elevation and LAI. LST bias increases strongly with soil moisture in croplands across all months, and moderately in savannas (April) and in barren and shrubland regions (April and October). With respect to elevation, bias increases strongly in forests (October), moderately to strongly in savannas (January and October), and moderately in grasslands (October). Croplands, on the other hand, show a moderate decrease in bias with elevation during January, April, and October, which, similar to nighttime patterns, may reflect the negative correlation between elevation and soil moisture (January: -0.74, April: -0.70, October: -0.39). LAI also plays a role, with bias moderately increasing with LAI in croplands (April and October), barren and shrubland regions (April), forests (October), and grasslands (October).

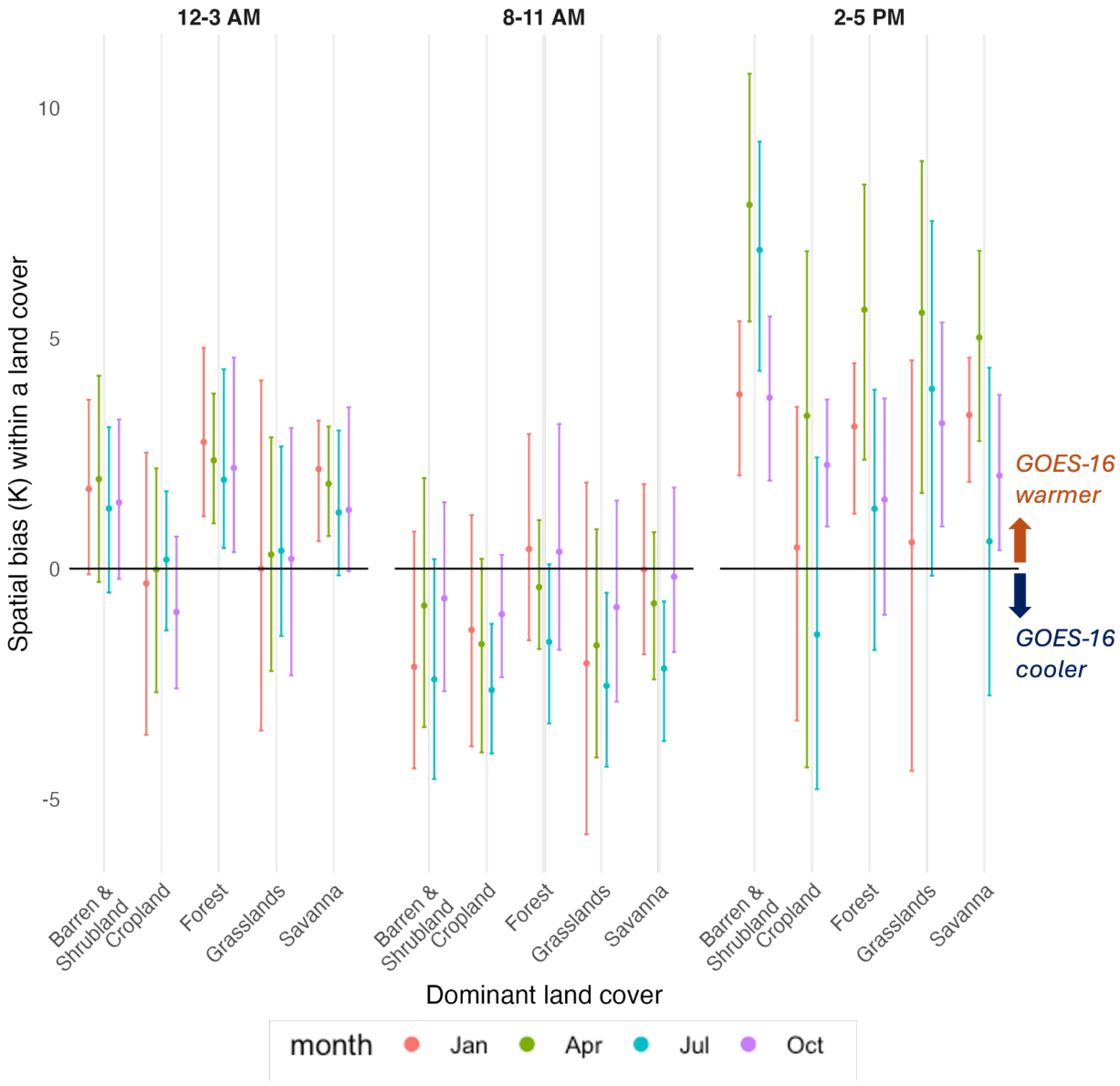

Figure 4. Spatial variation of bias between GOES-16 and MERRA-2 LST within individual land cover types. For each month, time period, and land cover, vertical lines indicate the 10th–90th percentile range of the spatial bias, while filled circles denote the mean. Substantial spatial variability in bias exists within land covers across daily and seasonal timescales.

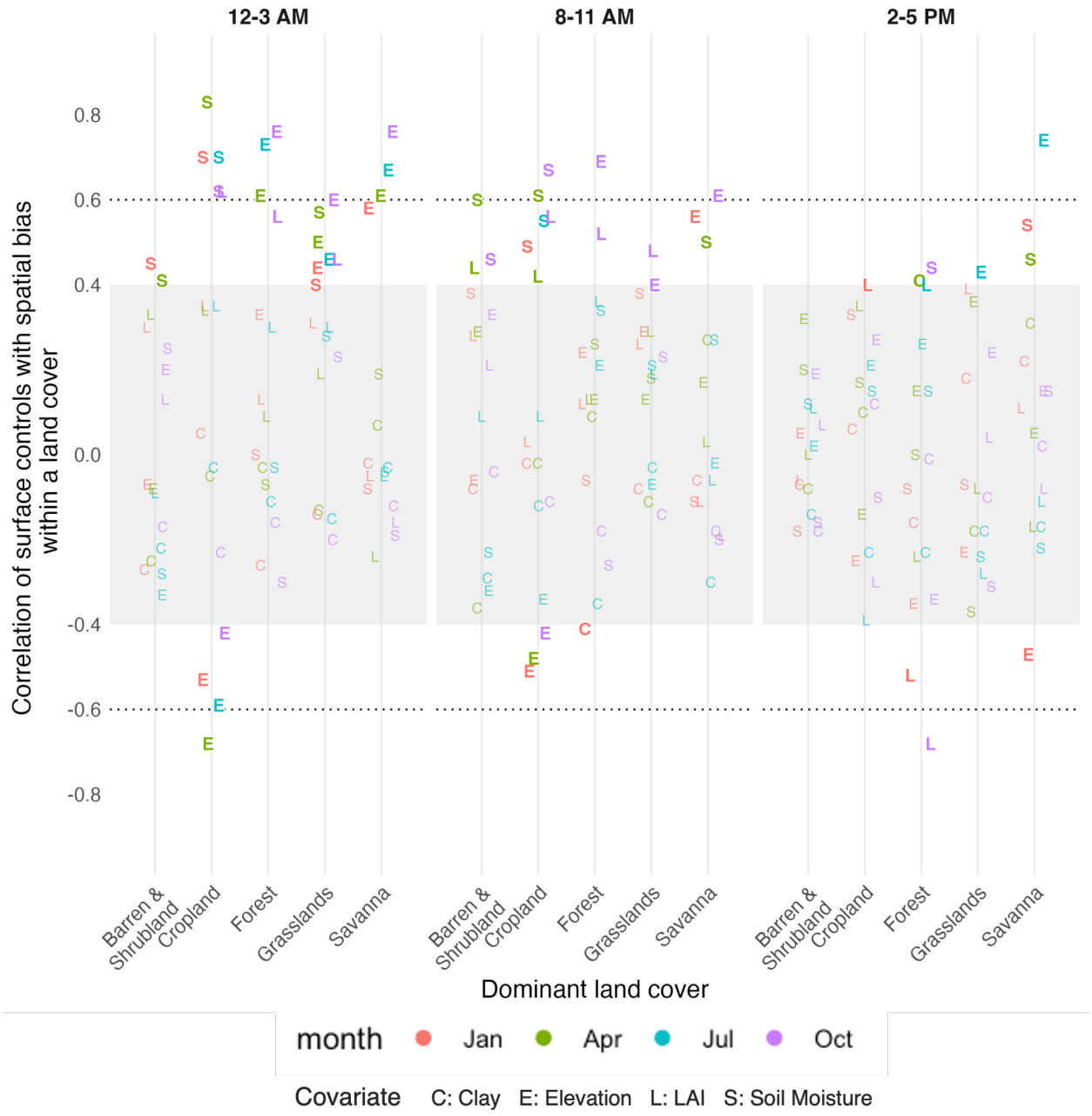

Figure 5 The spatial variability in bias is partly driven by differences in land surface controls within land cover types, including elevation, soil moisture, and Leaf Area Index (LAI). The association of these controls on bias, quantified using the Pearson correlation coefficient, varies with both time of day and season. We classify the association as moderate when the absolute correlation is between 0.4 and 0.6, and strong when greater than 0.6; values below 0.4 are shown in grey. At night, bias moderately to strongly increases with elevation (except over croplands) and soil moisture. In the morning, it increases with soil moisture, elevation (except over croplands), and LAI. By afternoon, the influence of surface controls is generally attenuated.

The influence of surface covariates on spatial variability of bias within a land cover is less pronounced in the afternoon compared to nighttime and morning periods. LAI effects are mixed: in forests, bias decreases moderately to strongly in January and October but increases moderately in July; in croplands, bias moderately increases with LAI in January. Elevation also plays a role, with bias moderately increasing in grasslands and strongly increasing in savannas during July. Unlike the nighttime and morning periods, soil moisture is not the dominant driver of spatial bias variability in the afternoon. However, bias moderately increases with soil moisture in savannas (January and April) and forests (October). Supporting Information (Table S1 and Table S2) lists the surface conditions that, for a given time period, month, and land cover, have a high percentage of pixels with an absolute bias greater than 2K.

We also analyzed the variability of these surface covariates within MERRA-2 pixels, using the standard deviation and coefficient of variation as metrics, but found no significant influence on the bias (not shown). Additionally, we compared the prescribed LAI product in MERRA-2 with the observed MODIS LAI product (500 m, 8-day MCD15A2H; (Myneni et al., 2021)) to determine whether pixel-wise differences between the two datasets contributed to biases. However, no significant patterns were identified. We conducted a similar comparison between MERRA-2 surface/root-zone soil moisture and the Soil Moisture Active and Passive (SMAP) Level-4 surface/root-zone soil moisture product (R. Reichle et al., 2018), but differences between these datasets also showed no relationship to the bias. Furthermore, we investigated whether differences in cloud cover between MERRA-2 and the GOES-16 were associated with consistent bias patterns between the two datasets, but no such patterns were observed.

6. Discussion

a. Mechanisms underlying bias differences between land covers

1. NIGHT

Our results indicate that GOES-16 LST is mostly warmer than MERRA-2 during nighttime across all seasons for barren & shrubland, forests, and savannas. For barren and shrubland pixels, we observe a warm bias in GOES-16 relative to MERRA-2, despite the expectation that nighttime radiative cooling typically results in cooler surface soil temperatures compared to

deeper layers (Campbell & Norman, 1998). Previous validation studies comparing GOES-16 LST data against SURFRAD in situ measurements at desert and shrubland sites reported that GOES-16 exhibited a negative bias (cooler) relative to SURFRAD (Yu, Tarpley, Xu, et al., 2012; Yu & Yu, 2020). Considering that MERRA-2 consistently appears cooler than GOES-16—when it would, in fact, be expected to be warmer due to GOES-16's established negative bias and MERRA-2 being representative of a deeper layer—our analysis suggests that MERRA-2 likely possesses a substantial negative bias at barren and shrubland locations during night relative to the true LST.

In densely forested regions in forests and savannas, GOES-16 LST primarily represents the canopy top, while MERRA-2 calculates LST based on the entire canopy depth and the top few centimeters of soil. Typically, forest canopies cool radiatively by emitting longwave radiation toward both the sky and the ground, resulting in a cooler canopy top relative to deeper canopy layers and underlying soil (Still et al., 2021), although some exceptions exist in colder climates (Staebler & Fitzjarrald, 2005). Contrary to expectations, our findings reveal that GOES-16 LST is warmer compared to MERRA-2. This discrepancy likely arises because critical biotic and abiotic factors influencing LST —e.g., leaf size, clumping, stomatal conductance, canopy structure and function (N. Dong et al., 2017; Jiang et al., 2019; Still et al., 2021)— are absent from the Catchment Land Surface Model, leading to compensating errors that bias MERRA-2 toward cooler values relative to GOES-16. This effect, however, is muted in croplands and grasslands.

2. MORNING

Since GOES-16 generally records warmer temperatures at night (except over croplands and grasslands), we expected GOES-16 to also be warmer than MERRA-2 during the morning period, given that the upper few millimeters of vegetation and soil typically warm faster than deeper subsurface layers during the morning (Campbell & Norman, 1998). However, our analysis reveals an opposite trend: GOES-16 is, on average, colder than MERRA-2 during morning hours, except over forests in January and October, where it is warmer. Several potential factors might explain these observations.

First, GOES-16 observes the contiguous United States at varying viewing angles, potentially altering the proportions of visible soil and vegetation fractions, thereby affecting the retrieved LST. Recent analysis by (Qin et al., 2025) using AmeriFlux sites indicated that GOES-16 morning LST retrievals exhibit higher root mean square errors compared to noontime retrievals, primarily due to sun-sensor geometry effects. They demonstrated that explicitly accounting for these angular variations significantly reduces errors. Second, the morning period corresponds to a longer atmospheric optical path length, increasing susceptibility to atmospheric absorption and emission of infrared radiation. Specifically, (S. J. Pestana et al., 2024) demonstrated that atmospheric absorption in midlatitude winter conditions could make the GOES-R Advanced Baseline Imager brightness temperature as much as 4 Kelvin colder than the true brightness temperature.

Conversely, for forests, where GOES-16 is typically warmer than MERRA-2 in January and October, prior studies suggest that this discrepancy arises from GOES-16 preferentially observing sunlit portions of trees (S. J. Pestana et al., 2024). This effect is most pronounced during winter mornings (and to a lesser extent in fall), when the angular difference between satellite viewing direction and solar illumination is small for the contiguous United States. At off-nadir angles, GOES-16 captures tree profiles rather than only the canopy top, and tree trunks exposed to insolation can become substantially hot (Rutter et al., 2023), especially under sparse canopy conditions (Pomeroy et al., 2009) common in fall and winter. Additionally, for pixels containing forests and snow, trees can obscure the snow surface beneath and behind them (S. Pestana et al., 2019), causing GOES-16 LST to appear warmer than the actual surface. Consequently, our findings emphasize the importance of incorporating improved angular radiometric corrections and explicitly accounting for enhanced warming in sunlit forested areas when comparing GOES-16 and MERRA-2 LST data during morning periods.

3. AFTERNOON

In general, GOES-16 is hotter in the afternoon than at night when compared with MERRA-2. This difference can be attributed to several factors, including uneven solar heating driven by

variations in sun-sensor geometry, surface topography, and thermal inertia; and increased thermal emission from exposed surfaces such as rocks and vegetation (Kuenzer & Dech, 2013) during the day. Across all seasons, GOES-16 consistently reports higher LSTs than MERRA-2 over bare lands and shrublands, with the largest discrepancies observed during the months of April and July. We hypothesize that this bias arises primarily from three factors. First, in dry sparsely vegetated regions, vertical temperature gradients within the soil column become more pronounced, with the top few millimeters substantially hotter than the underlying 5 cm layer (Holmes et al., 2008). Second, daytime LST retrievals over bare soil are more susceptible to errors related to surface emissivity variability than those over vegetated surfaces (Cheng & Liang, 2014; Jin & Liang, 2006; Ogawa et al., 2003). In addition, while directional effects of solar radiation on GOES-16 LST retrievals are generally reduced in the afternoon compared to the morning, these effects tend to be more prominent over sparsely vegetated areas (Carlson et al., 1995).

For croplands, the bias between GOES-16 and MERRA-2 LST is generally lower, particularly in April and July, likely due to frequent irrigation. We hypothesize that this reduction in bias is related to the increased thermal conductivity of wet soils, which reduces vertical temperature gradients near the surface. In July—when irrigation volumes are typically high due to elevated temperatures—the afternoon bias becomes negative. This may be attributed to the top few millimeters of the soil being significantly cooler than deeper layers due to irrigation-induced effects (Zhu & Burney, 2022). Another contributing factor is that the MERRA-2 Catchment Land Surface Model does not explicitly model irrigation, which may further contribute to the bias. Additionally, (L. Li et al., 2021)) found that GOES-16 LST consistently underestimated LST compared with in-situ observations for croplands in the US corn belt for midday time periods (10 AM - 2 PM) which might also explain this low bias for croplands between GOES-16 and MERRA-2.

Grasslands exhibit a pronounced afternoon bias during April and July, which generally correspond to the active growing season. By October, most grasslands enter senescence, while January represents the dormant phase with minimal vegetation activity across the United States (Fischer et al., 2023; Hartman et al., 2020). Accordingly, afternoon biases are highest in April

and July, lower in October, and negligible in January. These patterns suggest that the presence and growth stage of grasslands influence the observed bias between the two datasets, with greater bias occurring as grassland height and biomass increase. Our analysis indicates that the top few millimeters of the grassland canopy are significantly warmer than the combined grassland canopy and upper 5 cm of soil. This temperature difference amplifies during the growing season, decreases during senescence in the fall, and becomes negligible during dormancy in January.

Forests and savannas exhibit warmer temperatures during the afternoon; this is partly because GOES-16 senses only the top few millimeters of the canopy, which can be warmer than the deeper canopy layers. However, the magnitude of this bias varies seasonally. One possible explanation is that canopy structure strongly influences radiative transfer; in heterogeneous canopies, lower leaves can absorb radiation scattered from the upper layers (Roberts et al., 2004; Still et al., 2021). Additional factors such as leaf angle distribution and clumping also modulate within-canopy radiation absorption. In a forest, canopy temperature itself can vary considerably among species during the day (Zakrzewska et al., 2022). These results are supported by the strong impact of canopy structure representations on LST estimates in land surface models.

b. Influence of surface controls on bias

During the night and morning periods, our results indicate that bias variability within certain land covers—particularly croplands, and to a lesser extent, bare and shrublands and grasslands—is strongly influenced by surface soil moisture. In these regions, higher soil moisture levels are associated with GOES-16 LST being warmer than MERRA-2. One possible explanation is that the MERRA-2 soil moisture product, which we use in this study, represents an effective depth of 5 cm. This depth may not capture the wetness of the top few millimeters that directly influence GOES-16 LST, leading to biases between the two datasets under wetter conditions. Notably, the influence of soil moisture on bias variability becomes minimal in the afternoon, suggesting that at the MERRA-2 spatial resolution, vertical LST gradients within individual land cover types are less sensitive to surface soil moisture under high solar insolation, likely because the soil column dries more uniformly with depth as the day progresses. In croplands, an additional factor may be

the effect of irrigation: increased soil moisture from irrigation is not explicitly represented in the MERRA-2 Catchment Land Surface Model, potentially contributing to larger discrepancies between the two products at night and morning under wetter conditions, which are more likely to represent irrigated conditions than dry soil moisture levels are.

Elevation plays a significant role in modulating spatial LST bias variability within forests, savannas, and grasslands at night, while its influence is comparatively minor during the morning and afternoon. Our analysis shows that higher elevations are associated with GOES-16 LSTs being warmer than MERRA-2 during the night. Thermal infrared LST retrievals are known to have high errors in high-elevation regions with rugged topography due to pronounced surface heterogeneity and the effects of viewing geometry (Beale et al., 2020; Jia et al., 2023). Interestingly, compared to daytime thermal infrared retrieval errors, our results show that the effect of elevation on nighttime bias is more pronounced. This suggests that the bias is not solely due to insolation contrasts between sunny and shady slopes in mountainous regions, but also reflects the ways in which topography fundamentally alters water, energy, and biogeochemical processes (Hao et al., 2022). For instance, topography significantly influences lateral ridge-to-valley water transport (Fan et al., 2019), and north- and south-facing slopes often support different vegetation types, densities, and species compositions (Dearborn & Danby, 2017)—features that are generally poorly represented in land surface model parameterizations, including the Catchment Land Surface Model. Given that both GOES-16 and MERRA-2 exhibit limitations in high-elevation regions—particularly in complex terrain such as the Rocky Mountains, Colorado Plateau, and Sierra Nevada (as noted in Section 5.3.2)—our findings underscore the need to improve both thermal infrared-based retrieval algorithms and LST modeling to better capture topography-driven variability in LST.

Interestingly, contrary to our initial hypothesis, the effect of LAI within land cover types is less pronounced. Specifically, the effect of LAI on LST bias appears mainly during the night and morning hours of the spring and autumn seasons. We hypothesize that this seasonal pattern is largely due to the influence of temperature in controlling the onset of the growing season in spring and the timing of senescence in autumn. Multiple studies have shown that variability in temperature strongly affects the timing of leaf-out in spring and senescence in autumn (Gill et

al., 2015; Linderholm, 2006; Polgar & Primack, 2011). Land surface models have generally struggled to capture this interannual variability in phenological transition dates and related vegetation processes (Richardson et al., 2012). MERRA-2, which uses prescribed climatological LAI, cannot capture this variability, and this limitation may help explain why the influence of LAI is stronger during transitional seasons than in winter or summer.

7. Conclusion

This study provides a detailed evaluation of diurnal and seasonal biases between satellite-derived (GOES-16) and reanalysis-based (MERRA-2) LST across the contiguous United States, with particular emphasis on the role of land surface conditions in shaping these discrepancies. Our results show that GOES-16 typically exhibits a warm bias at night and during the afternoon, while displaying a cool bias in the morning. These patterns are primarily attributable to differences in averaging depth between thermal infrared retrievals and reanalysis skin temperature estimates, further modulated by soil moisture, elevation, and LAI.

We identify land cover as the dominant driver of LST bias, which explains a substantial portion of the spatial variability between the two datasets. Forests and savannas exhibit the strongest nighttime warm biases, whereas croplands display pronounced morning cool biases. Afternoon biases are most pronounced over barren and shrubland areas, driven by shallow surface heating and surface emissivity variability. Within individual land cover types, elevation and soil moisture exert strong controls on nighttime and morning biases, while vegetation phenology has a marked influence during transitional seasons (spring and autumn). By contrast, the role of surface controls in the afternoon is comparatively weaker due to the overriding effects of solar insolation.

Our findings underscore key limitations of both GOES-16 thermal infrared retrievals and MERRA-2 reanalysis in capturing sub-grid heterogeneity, complex canopy structures, and the influence of irrigation and topography on LST. Addressing these challenges—through improved angular corrections in thermal infrared retrieval algorithms, dynamic vegetation parameterizations in land surface models, and enhanced representation of sub-grid surface

heterogeneity—will be essential for effectively integrating satellite and reanalysis LST products in environmental applications, hydrological modeling, and numerical weather prediction. Ultimately, this work underscores that effectively reconciling remote sensing and reanalysis-based LST estimates requires capturing the evolving interplay among land cover, surface properties, and effective LST depth, which shifts markedly across the diurnal cycle and seasons.

Acknowledgments.

The authors were supported by a NASA Modeling, Analysis, and Prediction grant (80NSSC21K1523). AGK was also supported by the Alfred P. Sloan Foundation. We would also like to thank Rolf H. Reichle for his valuable inputs. The authors declare no conflict of interest.

Data Availability Statement.

The LST data used in this study were accessed from www.ncei.noaa.gov/airs-web and https://disc.gsfc.nasa.gov/datasets/M2T1NXRAD_5.12.4/summary?keywords=MERRA-2%20tavg1_2d_rad_Nx. The landcover and elevation data were accessed from https://appeears.earthdatacloud.nasa.gov. The percent clay data was accessed from https://www.nrcs.usda.gov/resources/data-and-reports/gridded-soil-survey-geographic-gssurgo-database.

References

Augustine, J. A., & Dutton, E. G. (2013). Variability of the surface radiation budget over the United States from 1996 through 2011 from high-quality measurements. Journal of Geophysical Research: Atmospheres, 118(1), 43–53. https://doi.org/10.1029/2012JD018551

664 Baatz, R., Hendricks Franssen, H. J., Euskirchen, E., Sihi, D., Dietze, M., Ciavatta, S., Fennel, K., Beck,
665 H., De Lannoy, G., Pauwels, V. R. N., Raiho, A., Montzka, C., Williams, M., Mishra, U., Poppe,
666 C., Zacharias, S., Lausch, A., Samaniego, L., Van Looy, K., … Vereecken, H. (2021). Reanalysis
667 in Earth System Science: Toward Terrestrial Ecosystem Reanalysis. Reviews of Geophysics,
668 59(3), e2020RG000715. https://doi.org/10.1029/2020RG000715
669 Bateni, S. M., Entekhabi, D., & Jeng, D.-S. (2013). Variational assimilation of land surface temperature
670 and the estimation of surface energy balance components. Journal of Hydrology, 481, 143–156.
671 https://doi.org/10.1016/j.jhydrol.2012.12.039
672 Beale, C., Norouzi, H., Sharifnezhadazizi, Z., Bah, A. R., Yu, P., Yu, Y., Blake, R., Vaculik, A., &
673 Gonzalez-Cruz, J. (2020). Comparison of Diurnal Variation of Land Surface Temperature From
674 GOES-16 ABI and MODIS Instruments. IEEE Geoscience and Remote Sensing Letters, 17(4),
675 572–576. IEEE Geoscience and Remote Sensing Letters.
676 https://doi.org/10.1109/LGRS.2019.2930174
677 Campbell, G. S., & Norman, J. M. (1998). Temperature. In G. S. Campbell & J. M. Norman (Eds.), An
678 Introduction to Environmental Biophysics (pp. 15–36). Springer New York.
679 https://doi.org/10.1007/978-1-4612-1626-1_2
680 Caparrini, F., Castelli, F., & Entekhabi, D. (2003). Mapping of Land-Atmosphere Heat Fluxes and
681 Surface Parameters with Remote Sensing Data. Boundary-Layer Meteorology, 107(3), 605–633.
682 https://doi.org/10.1023/A:1022821718791
683 Carlson, T. N., Taconet, O., Vidal, A., Gillies, R. R., Olioso, A., & Humes, K. (1995). An overview of the
684 workshop on thermal remote sensing held at La Londe les Maures, France, September 20–24,
685 1993. Agricultural and Forest Meteorology, 77(3), 141–151. https://doi.org/10.1016/0168-
686 1923(95)02258-Y
687 Cheng, J., & Liang, S. (2014). Estimating the broadband longwave emissivity of global bare soil from the
688 MODIS shortwave albedo product. Journal of Geophysical Research: Atmospheres, 119(2), 614–
689 634. https://doi.org/10.1002/2013JD020689

690 Dearborn, K. D., & Danby, R. K. (2017). Aspect and slope influence plant community composition more
691 than elevation across forest–tundra ecotones in subarctic Canada. Journal of Vegetation Science,
692 28(3), 595–604. https://doi.org/10.1111/jvs.12521
693 Dong, N., Prentice, I. C., Harrison, S. P., Song, Q. H., & Zhang, Y. P. (2017). Biophysical homoeostasis
694 of leaf temperature: A neglected process for vegetation and land-surface modelling. Global
695 Ecology and Biogeography, 26(9), 998–1007. https://doi.org/10.1111/geb.12614
696 Dong, S., Cheng, J., Shi, J., Shi, C., Sun, S., & Liu, W. (2022). A Data Fusion Method for Generating
697 Hourly Seamless Land Surface Temperature from Himawari-8 AHI Data. Remote Sensing,
698 14(20), Article 20. https://doi.org/10.3390/rs14205170
699 Fan, Y., Clark, M., Lawrence, D. M., Swenson, S., Band, L. E., Brantley, S. L., Brooks, P. D., Dietrich,
700 W. E., Flores, A., Grant, G., Kirchner, J. W., Mackay, D. S., McDonnell, J. J., Milly, P. C. D.,
701 Sullivan, P. L., Tague, C., Ajami, H., Chaney, N., Hartmann, A., … Yamazaki, D. (2019).
702 Hillslope Hydrology in Global Change Research and Earth System Modeling. Water Resources
703 Research, 55(2), 1737–1772. https://doi.org/10.1029/2018WR023903
704 Farr, T. G., & Kobrick, M. (2000). Shuttle Radar Topography Mission produces a wealth of data. Eos,
705 Transactions American Geophysical Union, 81(48), 583–585.
706 Fischer, F. M., Chytrý, K., Chytrá, H., Chytrý, M., & Těšitel, J. (2023). Seasonal beta-diversity of dry
707 grassland vegetation: Divergent peaks of above-ground biomass and species richness. Journal of
708 Vegetation Science, 34(2), e13182. https://doi.org/10.1111/jvs.13182
709 Freitas, S. C., Trigo, I. F., Macedo, J., Barroso, C., Silva, R., & Perdigão, R. (2013). Land surface
710 temperature from multiple geostationary satellites. International Journal of Remote Sensing,
711 34(9–10), 3051–3068. https://doi.org/10.1080/01431161.2012.716925
712 Friedl, M. A., & Davis, F. W. (1994). Sources of variation in radiometric surface temperature over a
713 tallgrass prairie. Remote Sensing of Environment, 48(1), 1–17. https://doi.org/10.1016/0034-
714 4257(94)90109-0

715 Friedl, M., & Sulla-Menashe, D. (2022). MODIS/Terra+ Aqua land cover type yearly L3 Global 0.05 Deg
716 CMG V061. NASA EOSDIS Land Processes Distributed Active Archive Center (DAAC) Data
717 Set, MCD12C1-061.
718 Gallego-Elvira, B., Taylor, C. M., Harris, P. P., & Ghent, D. (2019). Evaluation of Regional-Scale Soil
719 Moisture-Surface Flux Dynamics in Earth System Models Based on Satellite Observations of
720 Land Surface Temperature. Geophysical Research Letters, 46(10), 5480–5488.
721 https://doi.org/10.1029/2019GL082962
722 Gelaro, R., McCarty, W., Suárez, M. J., Todling, R., Molod, A., Takacs, L., Randles, C. A., Darmenov,
723 A., Bosilovich, M. G., Reichle, R., Wargan, K., Coy, L., Cullather, R., Draper, C., Akella, S.,
724 Buchard, V., Conaty, A., Silva, A. M. da, Gu, W., … Zhao, B. (2017). The Modern-Era
725 Retrospective Analysis for Research and Applications, Version 2 (MERRA-2).
726 https://doi.org/10.1175/JCLI-D-16-0758.1
727 Ghent, D., Kaduk, J., Remedios, J., Ardö, J., & Balzter, H. (2010). Assimilation of land surface
728 temperature into the land surface model JULES with an ensemble Kalman filter. Journal of
729 Geophysical Research: Atmospheres, 115(D19). https://doi.org/10.1029/2010JD014392
730 Gill, A. L., Gallinat, A. S., Sanders-DeMott, R., Rigden, A. J., Short Gianotti, D. J., Mantooth, J. A., &
731 Templer, P. H. (2015). Changes in autumn senescence in northern hemisphere deciduous trees: A
732 meta-analysis of autumn phenology studies. Annals of Botany, 116(6), 875–888.
733 https://doi.org/10.1093/aob/mcv055
734 Guillevic, P. C., Bork-Unkelbach, A., Göttsche, F. M., Hulley, G., Gastellu-Etchegorry, J.-P., Olesen, F.
735 S., & Privette, J. L. (2013). Directional Viewing Effects on Satellite Land Surface Temperature
736 Products Over Sparse Vegetation Canopies—A Multisensor Analysis. IEEE Geoscience and
737 Remote Sensing Letters, 10(6), 1464–1468. IEEE Geoscience and Remote Sensing Letters.
738 https://doi.org/10.1109/LGRS.2013.2260319

739 Gupta, P., Verma, S., Bhatla, R., Chandel, A. S., Singh, J., & Payra, S. (2020). Validation of Surface
740 Temperature Derived From MERRA-2 Reanalysis Against IMD Gridded Data Set Over India.
741 Earth and Space Science, 7(1), e2019EA000910. https://doi.org/10.1029/2019EA000910
742 Hao, D., Bisht, G., Huang, M., Ma, P.-L., Tesfa, T., Lee, W.-L., Gu, Y., & Leung, L. R. (2022). Impacts
743 of Sub-Grid Topographic Representations on Surface Energy Balance and Boundary Conditions
744 in the E3SM Land Model: A Case Study in Sierra Nevada. Journal of Advances in Modeling
745 Earth Systems, 14(4), e2021MS002862. https://doi.org/10.1029/2021MS002862
746 Hartman, M. D., Parton, W. J., Derner, J. D., Schulte, D. K., Smith, W. K., Peck, D. E., Day, K. A., Del
747 Grosso, S. J., Lutz, S., Fuchs, B. A., Chen, M., & Gao, W. (2020). Seasonal grassland
748 productivity forecast for the U.S. Great Plains using Grass-Cast. Ecosphere, 11(11), e03280.
749 https://doi.org/10.1002/ecs2.3280
750 Holmes, T. R. H., Owe, M., De Jeu, R. A. M., & Kooi, H. (2008). Estimating the soil temperature profile
751 from a single depth observation: A simple empirical heatflow solution. Water Resources
752 Research, 44(2). https://doi.org/10.1029/2007WR005994
753 Huang, L., Fang, X., Zhang, T., Wang, H., Cui, L., & Liu, L. (2023). Evaluation of surface temperature
754 and pressure derived from MERRA-2 and ERA5 reanalysis datasets and their applications in
755 hourly GNSS precipitable water vapor retrieval over China. Geodesy and Geodynamics, 14(2),
756 111–120. https://doi.org/10.1016/j.geog.2022.08.006
757 Inamdar, A. K., French, A., Hook, S., Vaughan, G., & Luckett, W. (2008). Land surface temperature
758 retrieval at high spatial and temporal resolutions over the southwestern United States. Journal of
759 Geophysical Research: Atmospheres, 113(D7). https://doi.org/10.1029/2007JD009048
760 Jia, A., Liang, S., & Wang, D. (2022). Generating a 2-km, all-sky, hourly land surface temperature
761 product from Advanced Baseline Imager data. Remote Sensing of Environment, 278, 113105.
762 https://doi.org/10.1016/j.rse.2022.113105
763 Jia, A., Liang, S., Wang, D., Ma, L., Wang, Z., & Xu, S. (2023). Global hourly, 5 km, all-sky
764 land surface temperature data from 2011 to 2021 based on integrating geostationary and polar-

765 orbiting satellite data. Earth System Science Data, 15(2), 869–895. https://doi.org/10.5194/essd-
766 15-869-2023
767 Jia, A., Liang, S., Wang, D., Mallick, K., Zhou, S., Hu, T., & Xu, S. (2024). Advances in Methodology
768 and Generation of All-Weather Land Surface Temperature Products From Polar-Orbiting and
769 Geostationary Satellites: A comprehensive review. IEEE Geoscience and Remote Sensing
770 Magazine, 12(4), 218–260. IEEE Geoscience and Remote Sensing Magazine.
771 https://doi.org/10.1109/MGRS.2024.3421268
772 Jiang, Y., Kim, J. B., Trugman, A. T., Kim, Y., & Still, C. J. (2019). Linking tree physiological
773 constraints with predictions of carbon and water fluxes at an old-growth coniferous forest.
774 Ecosphere, 10(4), e02692. https://doi.org/10.1002/ecs2.2692
775 Jin, M., & Liang, S. (2006). An Improved Land Surface Emissivity Parameter for Land Surface Models
776 Using Global Remote Sensing Observations. Journal of Climate, 19(12), 2867–2881.
777 https://doi.org/10.1175/JCLI3720.1
778 Kalma, J. D., McVicar, T. R., & McCabe, M. F. (2008). Estimating Land Surface Evaporation: A Review
779 of Methods Using Remotely Sensed Surface Temperature Data. Surveys in Geophysics, 29(4),
780 421–469. https://doi.org/10.1007/s10712-008-9037-z
781 Karnieli, A., Agam, N., Pinker, R. T., Anderson, M., Imhoff, M. L., Gutman, G. G., Panov, N., &
782 Goldberg, A. (2010). Use of NDVI and Land Surface Temperature for Drought Assessment:
783 Merits and Limitations. https://doi.org/10.1175/2009JCLI2900.1
784 Koster, R. D., Reichle, R. H., Mahanama, S. P. P., Perket, J., Liu, Q., & Partyka, G. (2020). Land-
785 Focused Changes in the Updated GEOS FP System (Version 5.25). GMAO Research Brief.
786 https://gmao.gsfc.nasa.gov/researchbriefs/land_changes_GEOS-FP/land_changes_GEOS-FP.pdf
787 Koster, R. D., Suarez, M. J., Ducharne, A., Stieglitz, M., & Kumar, P. (2000). A catchment-based
788 approach to modeling land surface processes in a general circulation model: 1. Model structure.
789 Journal of Geophysical Research: Atmospheres, 105(D20), 24809–24822.
790 https://doi.org/10.1029/2000JD900327

Kuenzer, C., & Dech, S. (2013). Theoretical Background of Thermal Infrared Remote Sensing. In C. Kuenzer & S. Dech (Eds.), Thermal Infrared Remote Sensing: Sensors, Methods, Applications (pp. 1–26). Springer Netherlands. https://doi.org/10.1007/978-94-007-6639-6_1

Lagouarde, J.-P., Ballans, H., Moreau, P., Guyon, D., & Coraboeuf, D. (2000). Experimental Study of Brightness Surface Temperature Angular Variations of Maritime Pine (Pinus pinaster) Stands. Remote Sensing of Environment, 72(1), 17–34. https://doi.org/10.1016/S0034-4257(99)00085-1

Li, L., Yang, Z.-L., Matheny, A. M., Zheng, H., Swenson, S. C., Lawrence, D. M., Barlage, M., Yan, B., McDowell, N. G., & Leung, L. R. (2021). Representation of Plant Hydraulics in the Noah-MP Land Surface Model: Model Development and Multiscale Evaluation. Journal of Advances in Modeling Earth Systems, 13(4), e2020MS002214. https://doi.org/10.1029/2020MS002214

Li, Z.-L., Wu, H., Duan, S.-B., Zhao, W., Ren, H., Liu, X., Leng, P., Tang, R., Ye, X., Zhu, J., Sun, Y., Si, M., Liu, M., Li, J., Zhang, X., Shang, G., Tang, B.-H., Yan, G., & Zhou, C. (2023). Satellite Remote Sensing of Global Land Surface Temperature: Definition, Methods, Products, and Applications. Reviews of Geophysics, 61(1), e2022RG000777. https://doi.org/10.1029/2022RG000777

Linderholm, H. W. (2006). Growing season changes in the last century. Agricultural and Forest Meteorology, 137(1), 1–14. https://doi.org/10.1016/j.agrformet.2006.03.006

Lu, Y., Steele-Dunne, S. C., Farhadi, L., & van de Giesen, N. (2017). Mapping Surface Heat Fluxes by Assimilating SMAP Soil Moisture and GOES Land Surface Temperature Data. Water Resources Research, 53(12), 10858–10877. https://doi.org/10.1002/2017WR021415

Ma, H., Zeng, J., Zhang, X., Fu, P., Zheng, D., Wigneron, J.-P., Chen, N., & Niyogi, D. (2021). Evaluation of six satellite- and model-based surface soil temperature datasets using global ground-based observations. Remote Sensing of Environment, 264, 112605. https://doi.org/10.1016/j.rse.2021.112605

Meng, C. L., Li, Z.-L., Zhan, X., Shi, J. C., & Liu, C. Y. (2009). Land surface temperature data assimilation and its impact on evapotranspiration estimates from the Common Land Model. Water Resources Research, 45(2). https://doi.org/10.1029/2008WR006971

Mira, M., Valor, E., Caselles, V., Rubio, E., Coll, C., Galve, J. M., Niclos, R., Sanchez, J. M., & Boluda, R. (2010). Soil Moisture Effect on Thermal Infrared (8–13-μm) Emissivity. IEEE Transactions on Geoscience and Remote Sensing, 48(5), 2251–2260. IEEE Transactions on Geoscience and Remote Sensing. https://doi.org/10.1109/TGRS.2009.2039143

Müller, B., Bernhardt, M., Jackisch, C., & Schulz, K. (2016). Estimating spatially distributed soil texture using time series of thermal remote sensing – a case study in central Europe. Hydrology and Earth System Sciences, 20(9), 3765–3775. https://doi.org/10.5194/hess-20-3765-2016

Myneni, R., Knyazikhin, Y., & Park, T. (2021). MODIS/Terra+Aqua Leaf Area Index/FPAR 8-Day L4 Global 500m SIN Grid V061 [Dataset]. NASA EOSDIS Land Processes Distributed Active Archive Center. https://doi.org/10.5067/MODIS/MCD15A2H.061

Norman, J. M., & Becker, F. (1995). Terminology in thermal infrared remote sensing of natural surfaces. Agricultural and Forest Meteorology, 77(3), 153–166. https://doi.org/10.1016/0168-1923(95)02259-Z

Ogawa, K., Schmugge, T., Jacob, F., & French, A. (2003). Estimation of land surface window (8–12 μm) emissivity from multi-spectral thermal infrared remote sensing—A case study in a part of Sahara Desert. Geophysical Research Letters, 30(2). https://doi.org/10.1029/2002GL016354

Olivera-Guerra, L.-E., Ottlé, C., Raoult, N., & Peylin, P. (2025). Assimilating ESA CCI land surface temperature into the ORCHIDEE land surface model: Insights from a multi-site study across Europe. Hydrology and Earth System Sciences, 29(1), 261–290. https://doi.org/10.5194/hess-29-261-2025

Peng, J., Ma, J., Liu, Q., Liu, Y., Hu, Y., Li, Y., & Yue, Y. (2018). Spatial-temporal change of land surface temperature across 285 cities in China: An urban-rural contrast perspective. Science of The Total Environment, 635, 487–497. https://doi.org/10.1016/j.scitotenv.2018.04.105

Pestana, S., Chickadel, C. C., Harpold, A., Kostadinov, T. S., Pai, H., Tyler, S., Webster, C., & Lundquist, J. D. (2019). Bias Correction of Airborne Thermal Infrared Observations Over Forests Using Melting Snow. Water Resources Research, 55(12), 11331–11343. https://doi.org/10.1029/2019WR025699

Pestana, S. J., Chickadel, C. C., & Lundquist, J. D. (2024). Thermal infrared shadow-hiding in GOES-R ABI imagery: Snow and forest temperature observations from the SnowEx 2020 Grand Mesa field campaign. The Cryosphere, 18(5), 2257–2276. https://doi.org/10.5194/tc-18-2257-2024

Polgar, C. A., & Primack, R. B. (2011). Leaf-out phenology of temperate woody plants: From trees to ecosystems. New Phytologist, 191(4), 926–941. https://doi.org/10.1111/j.1469-8137.2011.03803.x

Pomeroy, J. W., Marks, D., Link, T., Ellis, C., Hardy, J., Rowlands, A., & Granger, R. (2009). The impact of coniferous forest temperature on incoming longwave radiation to melting snow. Hydrological Processes, 23(17), 2513–2525. https://doi.org/10.1002/hyp.7325

Qin, B., Chen, S., Cao, B., Yu, Y., Yu, P., Na, Q., Hou, E., Li, D., Jia, K., Yang, Y., Hu, T., Bian, Z., Li, H., Xiao, Q., & Liu, Q. (2025). Angular normalization of GOES-16 and GOES-17 land surface temperature over overlapping region using an extended time-evolving kernel-driven model. Remote Sensing of Environment, 318, 114532. https://doi.org/10.1016/j.rse.2024.114532

Reichle, R., De Lannoy, G., Koster, R., Crow, W., Kimball, J., & Liu, Q. (2018). SMAP L4 Global 9 km EASE-Grid Surface and Root Zone Soil Moisture Land Model Constants, Version 4 [Dataset]. NASA National Snow and Ice Data Center Distributed Active Archive Center. https://doi.org/10.5067/KGLC3UH4TMAQ

Reichle, R. H., Draper, C. S., Liu, Q., Girotto, M., Mahanama, S. P. P., Koster, R. D., & Lannoy, G. J. M. D. (2017). Assessment of MERRA-2 Land Surface Hydrology Estimates. https://doi.org/10.1175/JCLI-D-16-0720.1

Reichle, R. H., Kumar, S. V., Mahanama, S. P., Koster, R. D., & Liu, Q. (2010). Assimilation of satellite-derived skin temperature observations into land surface models. Journal of Hydrometeorology, 11(5), 1103–1122.

Richardson, A. D., Anderson, R. S., Arain, M. A., Barr, A. G., Bohrer, G., Chen, G., Chen, J. M., Ciais, P., Davis, K. J., Desai, A. R., Dietze, M. C., Dragoni, D., Garrity, S. R., Gough, C. M., Grant, R., Hollinger, D. Y., Margolis, H. A., McCaughey, H., Migliavacca, M., … Xue, Y. (2012). Terrestrial biosphere models need better representation of vegetation phenology: Results from the North American Carbon Program Site Synthesis. Global Change Biology, 18(2), 566–584. https://doi.org/10.1111/j.1365-2486.2011.02562.x

Roberts, D. A., Ustin, S. L., Ogunjemiyo, S., Greenberg, J., Dobrowski, S. Z., Chen, J., & Hinckley, T. M. (2004). Spectral and Structural Measures of Northwest Forest Vegetation at Leaf to Landscape Scales. Ecosystems, 7(5), 545–562. https://doi.org/10.1007/s10021-004-0144-5

Rutter, N., Essery, R., Baxter, R., Hancock, S., Horton, M., Huntley, B., Reid, T., & Woodward, J. (2023). Canopy Structure and Air Temperature Inversions Impact Simulation of Sub-Canopy Longwave Radiation in Snow-Covered Boreal Forests. Journal of Geophysical Research: Atmospheres, 128(14), e2022JD037980. https://doi.org/10.1029/2022JD037980

Staebler, R. M., & Fitzjarrald, D. R. (2005). Measuring Canopy Structure and the Kinematics of Subcanopy Flows in Two Forests. Journal of Applied Meteorology, 44(8), 1161–1179. https://doi.org/10.1175/JAM2265.1

Staff, S. (2020). Gridded Soil Survey Geographic (gSSURGO) Database for the Conterminous United States. United States Department of Agriculture, Natural Resources Conservation Service.

Still, C. J., Rastogi, B., Page, G. F. M., Griffith, D. M., Sibley, A., Schulze, M., Hawkins, L., Pau, S., Detto, M., & Helliker, B. R. (2021). Imaging canopy temperature: Shedding (thermal) light on ecosystem processes. New Phytologist, 230(5), 1746–1753. https://doi.org/10.1111/nph.17321

Sun, D., & Pinker, R. T. (2004). Case study of soil moisture effect on land surface temperature retrieval. IEEE Geoscience and Remote Sensing Letters, 1(2), 127–130. IEEE Geoscience and Remote Sensing Letters. https://doi.org/10.1109/LGRS.2004.824749

Wang, D.-C., Zhang, G.-L., Zhao, M.-S., Pan, X.-Z., Zhao, Y.-G., Li, D.-C., & Macmillan, B. (2015). Retrieval and Mapping of Soil Texture Based on Land Surface Diurnal Temperature Range Data from MODIS. PLOS ONE, 10(6), e0129977. https://doi.org/10.1371/journal.pone.0129977

Wang, Y.-R., Hessen, D. O., Samset, B. H., & Stordal, F. (2022). Evaluating global and regional land warming trends in the past decades with both MODIS and ERA5-Land land surface temperature data. Remote Sensing of Environment, 280, 113181. https://doi.org/10.1016/j.rse.2022.113181

Watson, K. (1975). Geologic applications of thermal infrared images. Proceedings of the IEEE, 63(1), 128–137. Proceedings of the IEEE. https://doi.org/10.1109/PROC.1975.9712

Yu, Y., Privette, J. L., & Pinheiro, A. C. (2008). Evaluation of Split-Window Land Surface Temperature Algorithms for Generating Climate Data Records. IEEE Transactions on Geoscience and Remote Sensing, 46(1), 179–192. IEEE Transactions on Geoscience and Remote Sensing. https://doi.org/10.1109/TGRS.2007.909097

Yu, Y., Tarpley, D., Privette, J. L., Flynn, L. E., Xu, H., Chen, M., Vinnikov, K. Y., Sun, D., & Tian, Y. (2012). Validation of GOES-R Satellite Land Surface Temperature Algorithm Using SURFRAD Ground Measurements and Statistical Estimates of Error Properties. IEEE Transactions on Geoscience and Remote Sensing, 50(3), 704–713. IEEE Transactions on Geoscience and Remote Sensing. https://doi.org/10.1109/TGRS.2011.2162338

Yu, Y., Tarpley, D., Xu, H., & Chen, M. (2012). GOES-R Advanced Baseline Imager (ABI) Algorithm Theoretical Basis Document For Land Surface Temperature (Version 2.5). Noaa Nesdis Center For Satellite Applications And Research.

Yu, Y., & Yu, P. (2020). GOES-R Advanced Baseline Imager (ABI) Algorithm Theoretical Basis Document For Land Surface Temperature. Noaa Nesdis Center For Satellite Applications And Research.

Zakrzewska, A., Kopeć, D., Krajewski, K., & Charyton, J. (2022). Canopy temperatures of selected tree species growing in the forest and outside the forest using aerial thermal infrared (3.6–4.9 μm) data. European Journal of Remote Sensing, 55(1), 313–325. https://doi.org/10.1080/22797254.2022.2062055

Zhang, X., Tarpley, D., & Sullivan, J. T. (2007). Diverse responses of vegetation phenology to a warming climate. Geophysical Research Letters, 34(19). https://doi.org/10.1029/2007GL031447

Zhao, W., Wen, F., Wang, Q., Sanchez, N., & Piles, M. (2021). Seamless downscaling of the ESA CCI soil moisture data at the daily scale with MODIS land products. Journal of Hydrology, 603, 126930. https://doi.org/10.1016/j.jhydrol.2021.126930

Zhu, P., & Burney, J. (2022). Untangling irrigation effects on maize water and heat stress alleviation using satellite data. Hydrology and Earth System Sciences, 26(3), 827–840. https://doi.org/10.5194/hess-26-827-2022

Supporting Information for

Reconciling remote sensing and reanalysis land surface temperatures: How surface conditions shape bias between GOES-16 and MERRA-2 across the contiguous US

Dhruva Kathuria,[a,b] Alexandra G. Konings,[c] Jana Kolassa,[b,d,e] Yanlan Liu,[f,g] Meng Zhao,[h] Alexey N Shiklomanov[b]

[a] *GESTAR II, Morgan State University, Baltimore, MD*

[b] *Global Modeling and Assimilation Office, NASA Goddard Space Flight Center, Greenbelt, MD*

[c] *Department of Earth System Science, Stanford University, Stanford, CA*

[d] *Science Systems and Applications, Inc., Lanham, MD*

[e] *European Centre for Medium-Range Weather Forecasts, Bonn, Germany*

[f] *School of Environment and Natural Resources, The Ohio State University, Columbus, OH*

[g] *School of Earth Sciences, The Ohio State University, Columbus, OH*

[h] *Department of Earth and Spatial Sciences, University of Idaho, Moscow, ID*

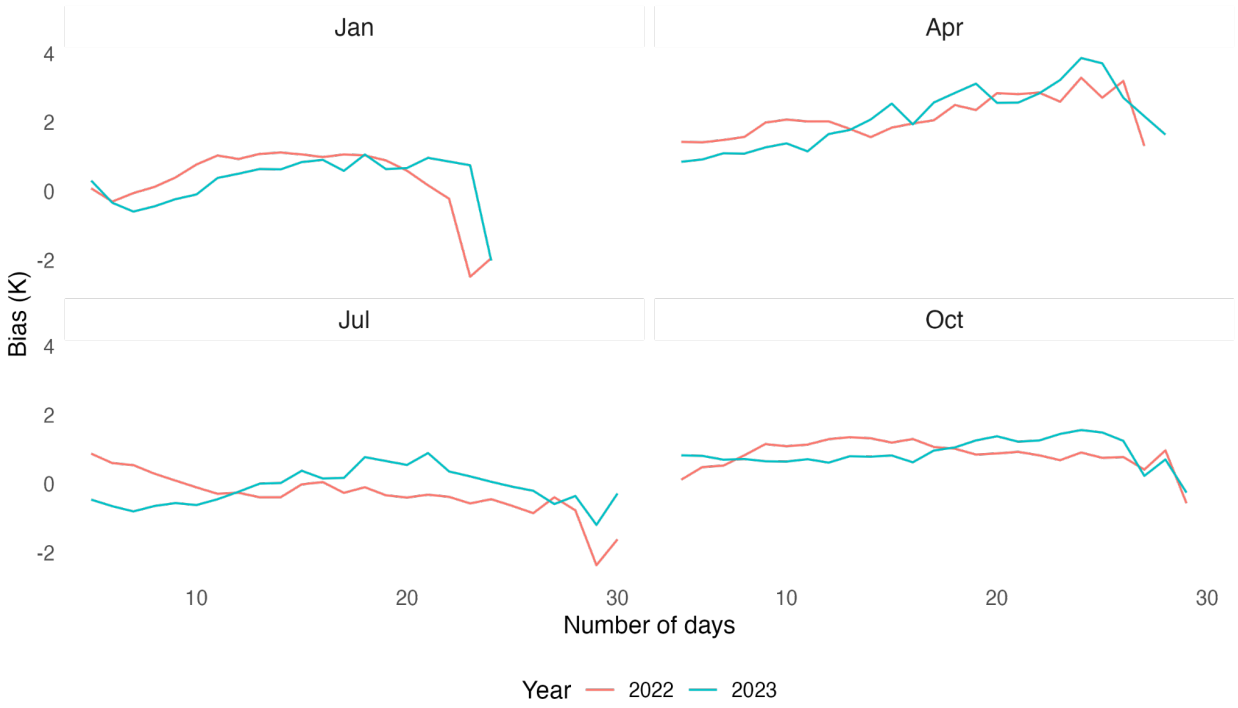

Figure S1. *Variation in the contiguous United States averaged bias with respect to the number of days of available observed data for a given pixel and hour. While a lower number of days could potentially introduce errors in bias estimation, the overall bias does not exhibit a significant change as the number of days increases from 5 to 30.*

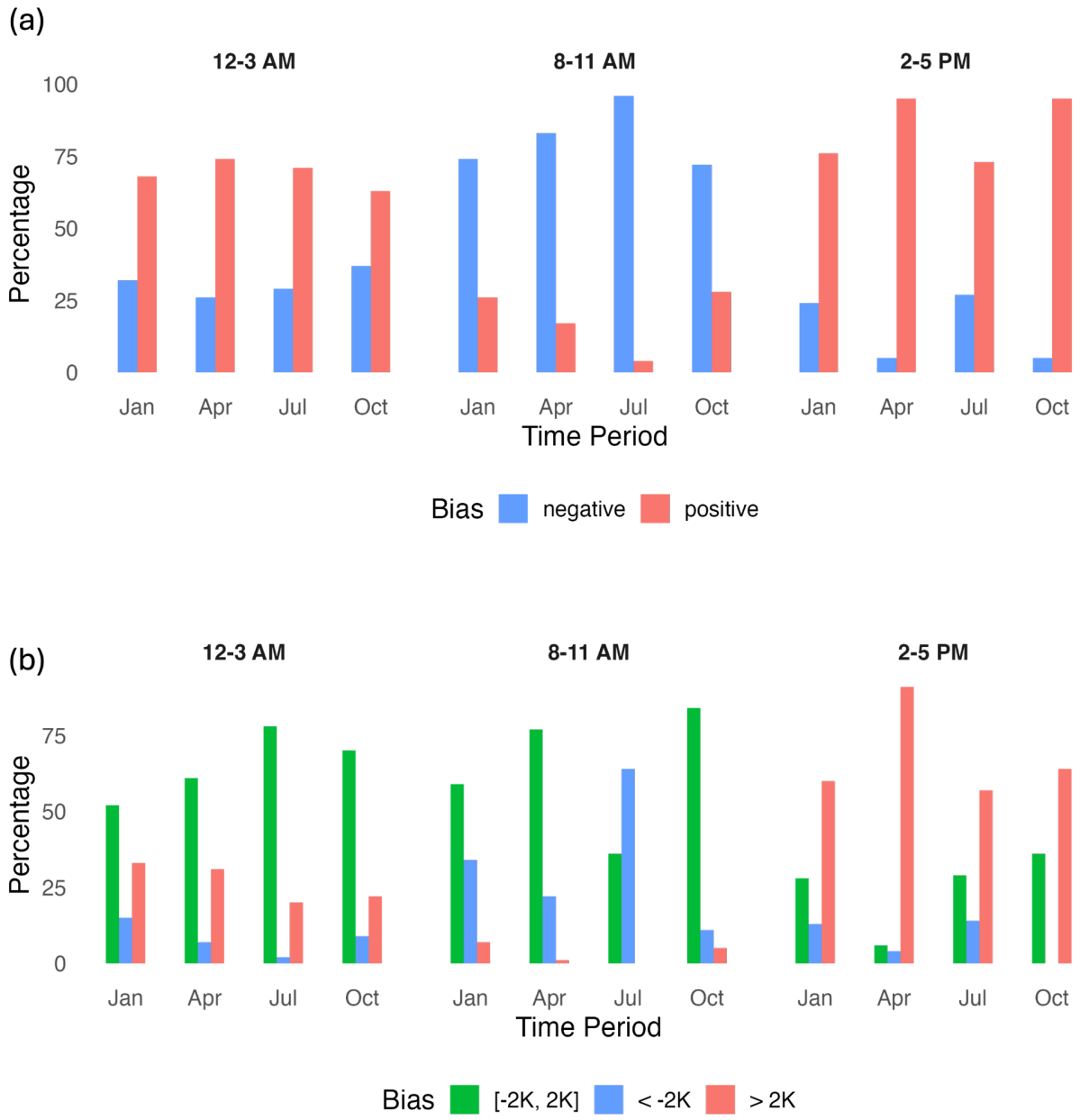

Figure S2. *(a) Percentage of pixels across contiguous United States with a positive bias (GOES-16 warmer than MERRA-2) or a negative bias (GOES-16 cooler than MERRA-2) averaged over the entire region. Nighttime and afternoon periods generally exhibit a positive bias, while morning periods show a negative bias. (b) Percentage of pixels with moderate bias (between −2K and 2K) or high absolute bias (less than −2K or greater than 2K). Afternoon periods have the highest percentage of pixels with a high positive bias.*

Table S1. *Pixels with specific surface conditions during a particular time period, month, and land cover that have a high percentage of pixels with an average bias less than −2K. Each cell consists of two rows: the first row describes the surface conditions of the pixels, while the second row provides the percentage of the pixels with these surface conditions which have a bias less than −2K, along with the average bias and the [10th quantile, 90th quantile] range of bias values. S: soil moisture, E: elevation, LAI: Leaf Area Index, C: Clay, B&S: Barren and Shrublands*

January			
	Night (12 AM - 3 AM)	**Morning (8 AM -11 AM)**	**Afternoon (2 PM-5 PM)**
Cropland	S < 0.2, E > 500m 65%; -2.5K [-4.3K, -0.7K]	S < 0.2, E > 500m 84%; -3.4K [-5.3K, -1.5K]	
Grassland		S < 0.2, 500m < E <1500m 83%; -3.8K [-6.2K, -1.6K]	
Forest			
Savanna			
Barren & Shrubland		S < 0.15 89%; -2.9K [-4.1K, -1.8K]	
April			
Cropland	S < 0.2, E >500m 78%; -2.6K [-3.7K, -1.3K]	S < 0.2, E > 500m 79%; -2.8K [-4K, -1.7K]	
Grassland			
Forest			

Savanna			
B&S			
July			
Cropland		S < 0.2, E > 250m 91%; -3.1K [-4K, -2K]	
Grassland		No relationship	
Forest		S <0.25, LAI < 6, C <8 71%, -2.4K [-3.5K, -1.4K]	
Savanna		S < 0.25, C > 15 79%; -2.6K [-3.7K, -1.5K]	E < 150m 63%; -2.3K [-4.2K, -0.8k]
Barren & Shrubland		E > 1000m 78%; -2.7K [-3.7K, -1.4K]	
October			
Cropland	S < 0.2, E > 500 58%; -2.1K [-3.5K, -0.8K]		
Grassland			
Forest			

Savanna			
Barren & Shrubland			

Table S2. *Pixels with specific surface conditions during a particular time period, month, and land cover that have a high percentage of pixels with an average bias greater than 2K. Each cell consists of two rows: the first row describes the surface conditions of the pixels, while the second row provides the percentage of the pixels with these surface conditions which have a bias greater than 2K, along with the average bias and the [10th quantile, 90th quantile] range of bias values. S: soil moisture, E: elevation, LAI: Leaf Area Index, C: Clay, B&S: Barren and Shrublands*

January			
	Night (12 AM - 3 AM)	**Morning (8 AM -11 AM)**	**Afternoon (2 PM-5 PM)**
Cropland	S > 0.3, EL < 150m 76%; 2.7K [1.5K, 3.7K]		S > 0.3 59%; 2K [0K, 3.6K]
Grassland	S>0.2, E > 1500m 59%; 3.4K [-0.4K, 7.8K]		E < 1000m, LAI > 0.5 95%; 3.7K [2.6K, 5K]
Forest	No relationship	C < 8% 53%, 1.8K [-0.7K, 4K]	E < 1000m, LAI < 4 92%; 3.4K [2.3K, 4.5K]
Savanna	E > 500m 68%; 4.4K [0.4K, 9.9K]		Most pixels (87%) are above 2K
B&S	S > 0.2 67%; 2.6K [0.5K, 4.5K]		Most pixels (90%) are above 2K

April			
Cropland			L > 0.5 96%; 5.1K [3.2K, 7K]
Grassland	S >0.2, E > 2000m 67%; 2.8K [0.8K, 5.2K]		Most pixels (89%) are above 2K
Forest	E > 500m 89%; 3.1K [2K, 4.2K]		C > 15 99%, 6.6K [3.8K, 8.3K]
Savanna	E > 500m 81%; 3.3K [1.2K, 5.2K]		Most pixels (93%) are above 2K
B&S	S > 0.15 72%; 2.7K [0.6K, 4.7K]		Most pixels (100%) are above 2K
July			
Cropland			
Grassland	E > 2000m, L > 1 63%; 2.7K [1K, 4.7K]		E > 1000m 86%; 4.9K [1.6K, 7.9K]
Forest	E > 500m 69%; 3.2K [1.1K, 5.2K]		S > 0.2, L > 5 66%; 2.4K [-0.5K, 4.3K]
Savanna	E > 500m 79%; 3.2K [1.1K, 4.9K]		E > 1000m 75%; 3.4K [0.9K, 5.9K]
B&S	No relationship		Most pixels (100%) are above 2K

October			
Cropland			L < 1.5 73%; 2.6K [1K, 4.1K]
Grassland	E > 2000m, L > 1 75%; 3.1K [1.2K, 4.9K]		S < 0.15 90%; 3.8K [1.9K, 5.6K]
Forest	E > 500m 87%; 3.7K [1.8K, 5.9K]		S > 0.2, L < 3 77%; 2.8K [1.5K, 3.9K]
Savanna	E > 500m 81%; 3.6K [1.3K, 5.6K]		No relationship
B&S	No relationship		Most pixels (90%) are above 2K

991
992
993
994
995